AFRL-AFOSR-VA-TR-2023-0195

Multi-functional Metafilms for Augmented Reality

Brongersma, Mark
LELAND STANFORD JUNIOR UNIVERSITY
450 SERRA MALL
STANFORD, CA,
US

11/22/2022
Final Technical Report

Air Force Research Laboratory
Air Force Office of Scientific Research
Arlington, Virginia 22203
Air Force Materiel Command

REPORT DOCUMENTATION PAGE

PLEASE DO NOT RETURN YOUR FORM TO THE ABOVE ORGANIZATION.

1. REPORT DATE	2. REPORT TYPE	3. DATES COVERED	
20221122	Final	START DATE 20191215	END DATE 20200914

4. TITLE AND SUBTITLE
Multi-functional Metafilms for Augmented Reality

5a. CONTRACT NUMBER	5b. GRANT NUMBER	5c. PROGRAM ELEMENT NUMBER
	FA9550-17-1-0331	61102F
5d. PROJECT NUMBER	**5e. TASK NUMBER**	**5f. WORK UNIT NUMBER**

6. AUTHOR(S)
Mark Brongersma

7. PERFORMING ORGANIZATION NAME(S) AND ADDRESS(ES)
LELAND STANFORD JUNIOR UNIVERSITY
450 SERRA MALL
STANFORD, CA
US

8. PERFORMING ORGANIZATION REPORT NUMBER

9. SPONSORING/MONITORING AGENCY NAME(S) AND ADDRESS(ES)	10. SPONSOR/MONITOR'S ACRONYM(S)	11. SPONSOR/MONITOR'S REPORT NUMBER(S)
Air Force Office of Scientific Research 875 N. Randolph St. Room 3112 Arlington, VA 22203	AFRL/AFOSR RTB1	AFRL-AFOSR-VA-TR-2023-0195

12. DISTRIBUTION/AVAILABILITY STATEMENT
A Distribution Unlimited: PB Public Release

13. SUPPLEMENTARY NOTES

14. ABSTRACT
The human vision system exhibits remarkable properties. For example, it can distinguish over 10 million colors and operate effectively over a luminance range of 1014. There are, however, many applications that require capabilities that surpass what humans can see with the naked eye. For example, seeing in darkness or foggy conditions or spotting of objects emitting/scattering light with specific spectral or polarization properties require enhanced vision. For this reason, enhanced vision devices and specialty cameras are essential tools in defense, law enforcement and first
responder scenarios. Currently, these devices tend to be very bulky and do not meet the size, weight, and power (SWaP) requirements that are desirable for wearables

15. SUBJECT TERMS

16. SECURITY CLASSIFICATION OF:			17. LIMITATION OF ABSTRACT	18. NUMBER OF PAGES
a. REPORT U	b. ABSTRACT U	c. THIS PAGE U	UU	30

19a. NAME OF RESPONSIBLE PERSON	19b. PHONE NUMBER *(Include area code)*
GERNOT POMRENKE	426-8426

Final Performance Report

Multi-functional Metafilms for Augmented Reality

FA9550-17-1-0331

12/15/2017 to 12/14/2020

Grantee Institution: **Stanford University**
476 Lomita Mall
Stanford, CA 94305

Program Manager: **Dr. Gernot Pomrenke,**
Tel: (703) 696-8426
Email: gernot.pomrenke@afosr.af.mil

Principal Investigator: **Dr. Mark L. Brongersma**
Tel: (650) 736 2152
Email: Brongersma@stanford.edu

Table of Contents

I. Executive summary

I.1. The key objectives and most important achievements of this program.

The human vision system exhibits remarkable properties. For example, it can distinguish over 10 million colors and operate effectively over a luminance range of 10^{14}. There are, however, many applications that require capabilities that surpass what humans can see with the naked eye. For example, seeing in darkness or foggy conditions or spotting of objects emitting/scattering light with specific spectral or polarization properties require enhanced vision. For this reason, enhanced vision devices and specialty cameras are essential tools in defense, law enforcement and first responder scenarios. Currently, these devices tend to be very bulky and do not meet the size, weight, and power (SWaP) requirements that are desirable for wearables. ***In this program, the Brongersma group worked on realizing multifunctional metasurfaces on transparent silica substrates to perform advanced filtering, imaging, and photodetection functions. Some of the metasurfaces were constructed from Mie resonant semiconductor (mostly Si) nanostructures. We also implemented new types of metasurfaces based on guided mode resonance (GMR) structures. The first type of metasurfaces can offer highly-local light scattering and photodetection functions within a subwavelength footprint, but with a low optical quality-factor (Q). The latter type of metasurface can provide very high-Q resonances, but the resonances are non-local (i.e. more delocalized/spread out spatially).*** Both types of metasurfaces are ultrathin and can thus be applied in regular eyeglasses or compact imaging systems.

At the start of the program, we developed subwavelength angle sensing detectors (***Nature Nanotechnology****, 13, 1143, 2018*) that can add functionality to imaging systems that typically only create maps of the light intensity[1]. We also developed new type of geometric phase metalenses (***Optics Express*** *26, 24835, 2018*) that enable imaging in a flat form factor[2]. Many of our subwavelength detectors employ optical Mie resonances in semiconductor nanostructures. Such resonances can selectively enhance the detection of light waves with a selected wavelength or state of polarization. In our research, we also found that we can control the spectral and polarization properties of these resonances by placing the nanostructures above a mirror (***Nano Letters****, 18, 3857, 2018*)[3]. Capitalizing on the knowledge we have built on Mie-resonant photodetectors and light scattering from nanowires, we were able to fabricate transparent multispectral photodetectors mimicking the human visual system (***Nature Communications*** *10, 4982, 2019*). Since they are transparent they can be applied to eyewear with getting noticed by a user.

Most of the detection mechanisms and metasurfaces have thus far been static, but in collaboration with the Shalaev group we have analyzed the opportunities for dynamic metasurfaces and these were discussed in a highly cited review in Science (***Science 364***, eaat3100, 2019). This work also played into the MURI efforts led by Federico Capasso and Andrea Alu.

In the later stages of the program we pursued new approaches to imaging by capitalizing on our knowledge of both nanoscale photodection schemes and novel metasurface-based flat optics. For example, we have developed the first light-field metasurface and demonstrated its potential in high-resolution single-particle tracking experiments (***Nano Letters****, 19, 2267, 2019*). We have also developed dynamic metasurfaces based on phase change materials to ultimately allow the use of dynamic metasurfaces in imaging (***Advanced Optical Materials*** 2000745, 1, 2020). Together with the Dionne group we developed non-local, high-*Q* metasurfaces that allow beam steering of select

wavelengths (***Nature Nanotechnology***, 15, 956, 2020). Whereas the Dionne group is currently exploring the use of these unique metasurfaces in non-linear optics and sensing, we have applied it to imaging and tracking of the motion of the human eye (In press at ***Nature Nanotechnology***, 2021). To explore the ultimate scaling limits for flat optics, we have also demonstrated the possibility to create atomically-thin and tunable lenses created from 2-dimensional semiconductors (***Nature Photonics*** *14, 426, 2020*).

This very successful program with a number of high impact Nature (5) and Science (1) publications has provided many new insights into the operation and possible uses of novel, nanostructured photodetection and imaging systems. The most recent works on eye tracking and atomically-thin lenses has also highlighted the great potential for the use of atomically-thin materials in flat optics. These materials enable extreme tunability and new optical properties that can be used in ultrathin light sources, modulator, photodetection and beam steering systems. In this final report, we describe our most important findings and pay special attention to the most recent efforts.

II. Research Accomplishments

II.1. Subwavelength angular sensors

Sensing the direction of sounds gives animals clear evolutionary advantages as it helps to find mates, locate preys, and avoid predators. Small animals like crickets, flies, and geckos cannot rely on large interaural differences to localize sounds in an auditory scene. For decades, biologists, neuroscientists and physicists have tried to elucidate why these animals nonetheless exhibit excellent directional hearing. Recent studies have revealed an intricate angle-sensing mechanism that is completely different from those seen in large animals and relies on the coherent coupling of soundwaves in two 'ears'. In a collaboration with the groups of Shanhui Fan at Stanford and Zongfu Yu at the University of Wisconsin, we applied this mechanism to electromagnetic waves by demonstrating the effective use of a pair of electrically-isolated but optically-coupled photodetectors. Exploiting the non-Hermitian interactions resulting from a mediation through the continuum, resonant photodetectors can accurately differentiate incident angles using a subwavelength footprint. This work breaks the limitation of conventional photodetectors that only sense light intensity and lose all phase information in an incoherent detection process.

Imaging chips are constructed from a large array of photo-detecting pixels. Conventional pixels only detect the intensity of light and are incapable of acquiring other important information, such as the incident angle of the light. While the intensity information alone is sufficient for traditional applications, such as photography, its limitation becomes apparent in advanced imaging tasks. For example, a single image of the intensity cannot reveal depth-information of objects in a scene, which requires directional information. Another example is the light-field camera, which uses information from incident angles to refocus even after the image is taken. To measure the incident angle, one has resorted to discrete optical components such as lenses or gratings together with photo-detecting pixels. These components are expensive to integrate and degrade the resolution. Only recently, have researchers been able to successfully integrate angle-sensitive pixels (ASPs) into a CMOS architecture. Their minimum size has been on the order of several microns as their operation relies on the use of gratings. With current scaling trends for imaging systems, the size of pixels is rapidly approaching the optical wavelength λ_0 This poses a seemingly

unsurpassable challenge towards angle detection. Existing methods based on micro-lenses or gratings cannot be miniaturized indefinitely because diffraction effects will result in a decrease in the accuracy of the angular measurement. Figure 1a illustrates this point for a system that uses a lens to measure the incident angle by focusing light of different directions to distinct spatial locations. The measurement accuracy is reduced by the diffraction-limited spot size in the focus, which scales as $\Delta\theta \sim \lambda_0/dcos(\theta)$. Consequently, when the lens' diameter d decreases below λ_0, the accuracy degrades severely. This accuracy can be quantified in terms of a minimum detectable angle change $\delta\theta$ that is ultimately limited by the presence of noise. In this work, we demonstrate that non-Hermitian coupling between neighboring photodetector elements can be exploited to for the first time realize an intrinsically subwavelength-sized ASP with a $\delta\theta$ = 0.24 degrees. Such a small $\delta\theta$ would be unimaginable for a subwavelength pixel without this type of optical coupling.

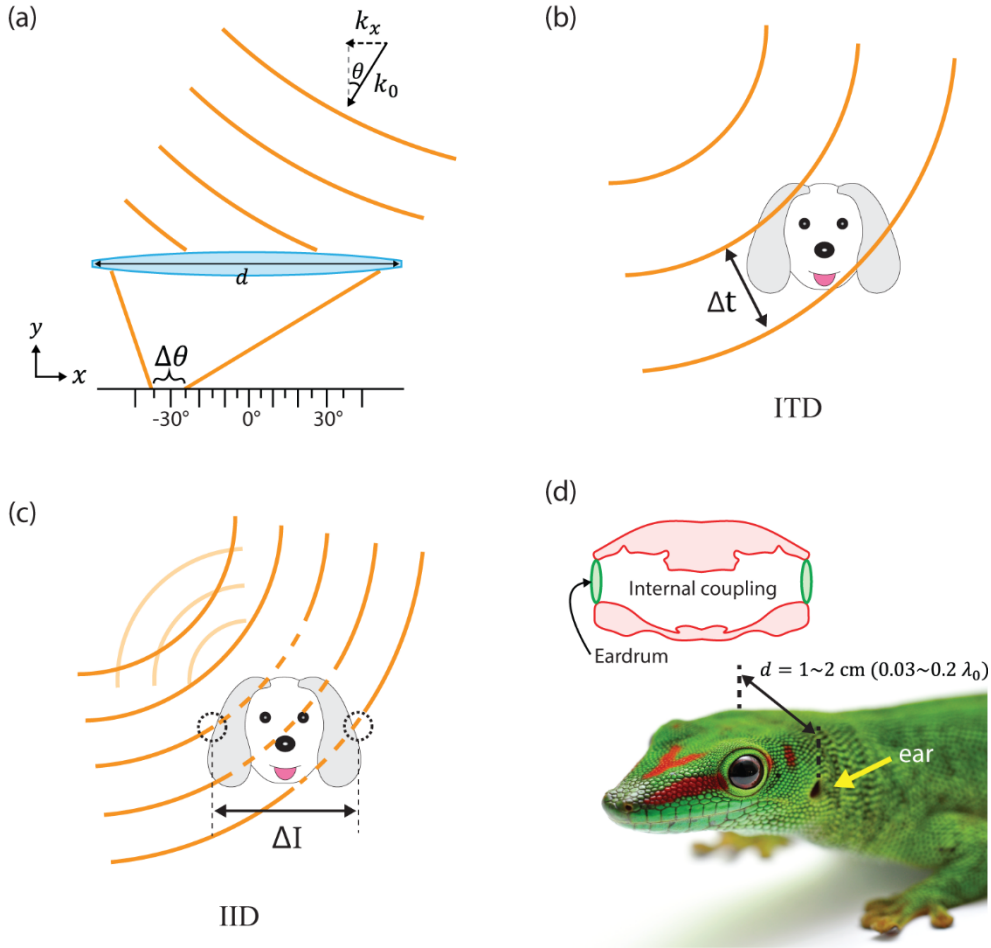

Fig.1. (a) Concept of incident angle detection using a lens with a diameter d that produces a finite-sized spot in its focal plane when illuminated by an off-axis, collimated beam. The angular spread $\Delta\theta$ resulting from diffraction limits the minimum detectable angle change given a limited signal-to-noise ratio in a real optical measurement. (b) and (c) Directional hearing of animals based on the detection of an interaural time difference (ITD) or interaural intensity difference (IID). Δt is the arrival time difference and ΔI is the intensity difference between two ears. (d) Head structure of a gecko showing internal coupling between two eardrums. The distance d between two ears is typically 1 to 2 cm and thus on a subwavelength scale with respect to audible sound wavelengths in the range from 8.5 - 34 cm.

A similar challenge in the miniaturization of angle sensors is encountered in a completely different context: directional hearing in animals. Using two *independent* ears, large mammals can easily determine the incident angle of sound based on two well-understood mechanisms as illustrated in Fig. 1b-c. The first relies on the interaural time difference (ITD) of the arrival time of the sound. The second method, the interaural intensity difference (IID) measures the intensity difference caused by the shadow of the body. Both mechanisms completely fail in small animals of subwavelength sizes. The ITD becomes too small to detect directly from the timing between neural spikes. The IID also diminishes as the shadow of a subwavelength body is blurred by wave diffraction. How small animals achieve directional hearing has been a subject of intense research and debate for many years. It is believed that the signals acquired by two ears need to couple, in great contrast to the essentially independent ears used by large animals. For example, a gecko uses a tunnel through the head to acoustically couple two eardrums (Fig. 1d). Acoustic simulations suggest that this coupling greatly amplifies interaural differences.

Closely following the design of the auditory system in small animals, we designed a subwavelength photodetection pixel that can measure both the intensity and the incident angle of light. It consists of two nanoscale optical resonators, which serve the equivalent role of the two eardrums (Fig. 2a). In our case, two Si nanowires serve as the optical resonators. They can internally circulate light to produce standing electromagnetic waves in an analogous way as an eardrum hosts standing mechanical vibrations. Because of the high refractive index of semiconductors, the sizes of resonators and their separation can be much smaller than the free-space optical wavelength. Such small separations and good detection efficiencies have been impossible with conventional, non-resonant detectors. By electrically contacting each nanowire to form photodetectors, they afford measurement of the internally stored optical energy through simple photocurrent measurements.
We demonstrated that the two electrically-isolated and optically-coupled photodetectors allow angle-sensing by monitoring the difference in stored energy between the resonators. Figure 2a shows the schematic of a fabricated device. Gold electrodes cover the two ends of each nanowire to form two photodetectors. These two photodetectors are electrically isolated from each other, but optically coupled. Two photocurrents can be measured from this four-terminal device. The difference in photocurrent is proportional to the difference in light absorption, which tells the incident angle of light. Figure 2b shows a scanning electron microscope (SEM) image of the device. For the fabrication, a lightly n-doped Poly-Si is deposited on a glass substrate, followed by electron beam lithography to define the nanowires and gold contacts. The inset shows a close-up view of the 105-nm-wide (A and C) nanowires separated by an equally large gap (B). Each nanowire forms a photoconductive detector whose resistance changes upon illumination. To characterize the optical resonance in the nanowires, we measure the spectra of the photocurrent for normally-incident light. Both the transverse magnetic (TM in Fig. 2c) and the transverse electric (TE in Fig. 2d) polarizations we can see a resonant peak in the visible wavelength range.

We measure the angular response at the wavelength of 550 nm. For TM polarization, the photocurrent ratio increases from 1 to 3 as the incident angle increases from 0° to 70° (Fig. 2e). For TE polarization, the photocurrent ratio increases monotonically up to 45° (Fig. 2f). In both cases, the experimental results agree with the full-wave simulations (solid lines Fig. 2e-f) very well. The peak in Fig. 2f is created by the unique radiation profile of the TE superradiant eigenstate. This detector can work for unpolarized light by confining the field of view (FOV) to $\pm 45°$, sufficient for many applications.

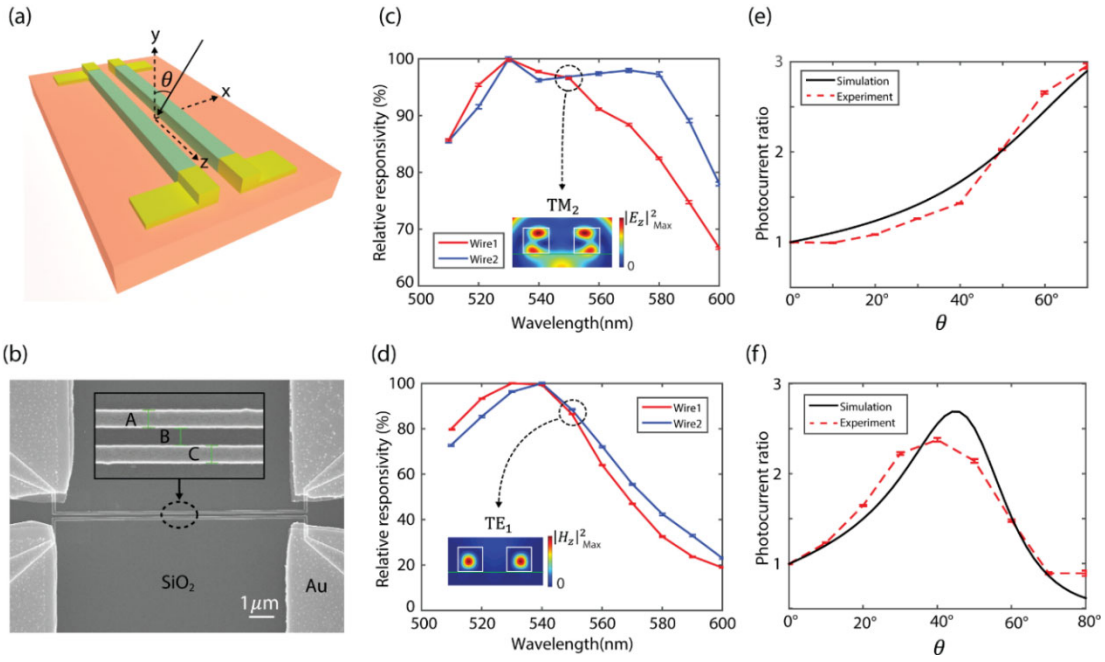

Fig. 2. (a) Schematic of an angle-sensing photodetector. (b) Scanning electron microscope image of fabricated angle sensing photodetector. Top inset shows a close-up view where A=105 nm, B=105 nm and C=103 nm. (c) Normalized responsivity of two nanowires with electric field polarized in z-direction. The responsivity is defined as R=I/P, where *I* is the measured photocurrent; P is the incident power. Inset shows the electric field intensity for TM_2 mode. (d) Normalized responsivity of two nanowires with magnetic field polarized in z-direction. Inset shows the magnetic field intensity for TE_1 mode. (e) Photocurrent ratio between two nanowires as a function of θ with the same polarization as in (c). (f) Photocurrent ratio between two nanowires as a function of θ with the same polarization as in (d).

One immediate application of angular photodetectors is depth-sensing. As a demonstration, we use two angle-sensing photodetectors to triangulate the position of a light emitting diode (LED). A top view photograph of the experimental setup is provided in Fig. 3a. It shows the photodetectors and LED as placed in the same horizontal plane. The LED light source has a center wavelength of 520 nm. A chopper is used together with a lock-in amplifier to measure the photocurrent. Two angle-sensing detectors are mounted on two chips separated by 50 mm. A top view schematic is shown in Fig. 3b. All coordinates are in the unit of millimeter. Using triangulation, the location of the LED during movement, including both the lateral position *x* and the depth *y*, can be obtained from the measured incident angles $\Theta_{1,2}$ for the LED light falling onto the two angle sensors:

$$(x, y) = \left(\frac{(tan\Theta_1)x_1 - (tan\Theta_2)x_2}{tan\Theta_1 - tan\Theta_2}, \frac{tan\Theta_1 \cdot tan\Theta_2}{tan\Theta_1 - tan\Theta_2} \cdot (x_1 - x_2) \right)$$

where $x_{1,2}$ are the coordinates of the two detectors. Θ in Eq. (2) is defined with respect to horizontal plane i.e. $\Theta = 90°$ for normal incidence.

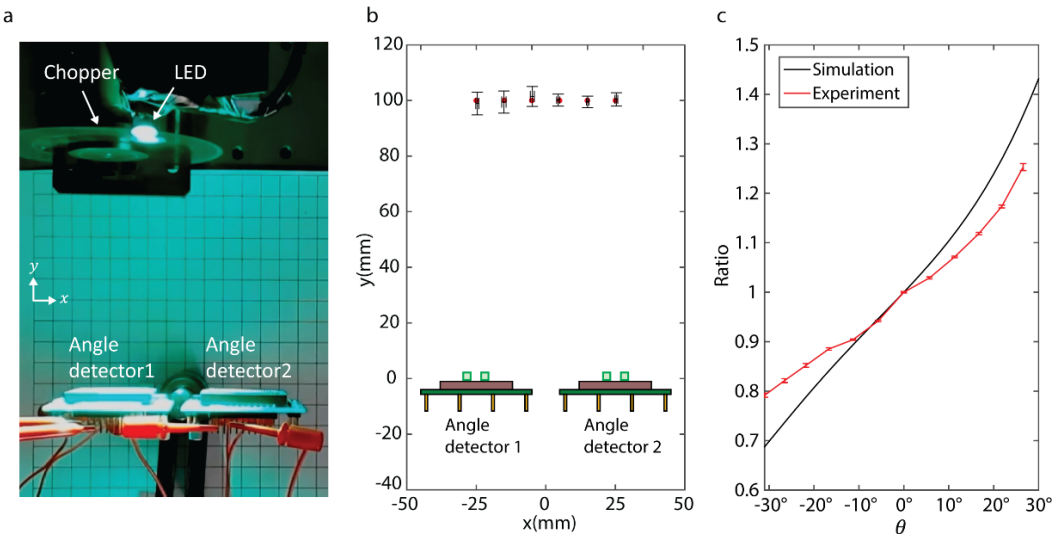

Fig. 3. Measurement setup and experimental results for lens-less positioning. a, Two angle-sensing detectors mounted on two separate chips are placed 50mm away from each other in x-direction. A light emitting diode (LED) light source embedded in a hemispherical glass lens with a diameter of 5.6 mm is placed 100mm away in y-direction from two angle-sensing detectors. A chopper and a lock-in amplifier is used to measure the photocurrent of nanowires in two angle-sensing detectors. Measurement is done at six different LED locations that are separated 1 cm equally from neighboring locations. 1cm square grid paper is placed on the bottom as a scale. **b,** LED position uncertainty in x- and y-direction for six discrete measurements in 2D plane where the red dots represent the true location of LED light source. Error bars are generated using 50 measurements at each location with propagation of uncertainty method for Eq. 2. LED is assumed as a point source for calculation. **c,** Full-wave simulation and experimentally measured photocurrent ratio under unpolarized light.

In the experiment, we first characterize the angular response of an individual angle-sensing photodetector under LED illumination up to angles of $\pm 30°$. A monotonic angular profile is obtained (red line in Fig. 3c), in agreement with the full-wave simulation results (black line in Fig. 3c) for unpolarized light. Using the experimental curve as the calibration, we measure the incident angles $\Theta_{1,2}$ of the light and then use Eq. (2) to estimate the location of the LED. The black markers in Fig. 3b show the calculated LED positions while the red markers show its true locations. The triangulation provides an excellent measurement of the location of light source.

Compared to existing depth sensing methods based on time-of-flight or stereo cameras, angular photodetectors provide a much simpler solution to depth-sensing. It can reach centimeter accuracy for a range up to ten meters, which is comparable to leading commercial depth sensors. More importantly, it does not use any lenses or require time synchronization.

The minimum detectable angle change is determined by the contrast ratio for the photocurrent as well as the signal-to-noise ratio (*SNR*) of the photodetector. For near-normal incidence, the minimum detectable angle change can be calculated as $\delta\theta = \frac{2}{SNR}\frac{\theta_{max}}{R_{max}-1}$ assuming a linear angular dependence that has a dynamic range up to θ_{max} degree and a maximum contrast ratio of R_{max} (See derivation in SI section 14). In our measurement, we obtain a maximum *SNR* of 28 dB by using a lock-in amplifier and averaging over multiple measurements. This *SNR* leads

to a $\delta\theta$ of 0.32 degree. Our detectors are photoconductors, which are known to have high noise levels. Future experiments could employ photodiodes together with integrated amplification circuits to greatly reduce noise. For example, using CMOS image sensing technology a typical *SNR* of 43.4 dB can be reached and this leads to a $\delta\theta$ of 0.009 degrees.

II.2. Limitations and opportunities for angle-sensitive detectors and imaging

Since the geometry of two nanowires represents a faithful imitation of the coupled ears of small animals, it also inherits the same limitations found in the biological world, including a limited operational bandwidth, lack of full azimuth and elevation angle capability, and a difficulty in differentiating multiple incoming waves. The limitations of these natural designs can be overcome. For example, by using two pairs of angle detectors orientated orthogonally, one can detect both azimuth and elevation angles. One can also use multiple (instead of two) resonant detectors to expand the bandwidth of operation and to differentiate multiple incident waves. When densely fabricated in arrays, these resonance-based angle sensors also need to be spaced by a minimal distance to avoid inter-pixel coupling.

With this newly accessible information about the intrinsic properties of light, angle-sensing pixels can be created for imaging chips that enable a wide variety of new applications for advanced light sensing. For example, the angular information of light may provide better scene awareness for autonomous systems such as self-driving cars and sun-tracking solar panels. Furthermore, electrically-isolated and optically-coupled photodetectors could further be made to perform multi-modal sensing for polarization and wavelength. These light sensors extract highly specific information from the environment and could become pervasive in next-generation smart optoelectronic systems.

II.3. High-quality-factor metasurfaces and an application in eye tracking

With the Dionne group we developed non-local, high-Q metasurfaces that allow beam steering of select wavelengths. These metasurfaces appear to have many important applications and we used them for optical eye-tracking. Such systems have been plagued by what seemed intrinsic properties of gratings. It is well-established that periodic gratings only propagate zeroth-order transmitted and reflected beams in the long wavelength limit where the wavelength-to-period ratio is sufficiently large. Newly emerging eye-tracking systems in eyewear require opposite, seemingly unphysical behavior from the embedded grating elements. Here, gratings need to redirect near-infrared light to image the eye and freely pass shorter wavelength visible light without diffraction to avoid the formation of unwanted rainbows. We demonstrate that a high-quality-factor (high-Q) guided-mode-resonator metasurface can accomplish this feat by providing unparalleled spectral control over the relative importance of the absorption and scattering by its grating elements. The creation of this conceptually new type of optical component required the fabrication of atomically-thin gratings across macroscopic, centimeter-scale areas.

Wearable technologies are home to a microcosm of optical devices that have to efficiently work together to perform a complex set of display, sensing, imaging, filtering, computation, and illumination functions. The need for wearables to be lightweight, fashionable, and operate at high speed and low power is putting very demanding

requirements on the optical elements. Nanostructured optical coatings termed metasurfaces [4,5] are presenting some solutions by offering a compact form-factor, multi-functionality [6,7], very high-numerical apertures [8,9], minimal aberrations [10–12], control over the light field [13,14], and facile integration with electronics. However, the recent development of eye-tracking (ET) for augmented reality systems has prompted some of the most thought-provoking optics design challenges for which even metasurface-based flat optics does not appear to have solutions.

ET hardware finds a wide range of applications in medicine, psychology and neuroscience, marketing research, sports, and gaming [15,16]. It senses the eye's gaze and pupil size to optimize a user experience or functions as a human-computer interface to more naturally control mechanical and virtual systems. Early attempts to perform ET date back to the late 19th century, when highly invasive mechanical setups were employed [17,18]. Optical ET techniques have recently emerged as the most accurate and a number of commercial systems are on the market. They follow the eye's motion by illuminating it with a near-infrared, light-emitting diode (NIR-LED) and capturing the light reflected from the cornea with a high-speed camera. Imaging algorithms are then used to assess the gazing direction. ET in eyewear or augmented reality systems requires the placement of optical elements directly in front of the eye and these tend to be bulky and disturb the user's view. Grating structures patterned on glasses have been proposed as a compact solution to image and track the eye's motion through a diffracted order. However, even the most subtle lined gratings and advanced holographic gratings unavoidably produce diffracted beams in the visible (VIS) spectral range (i.e. rainbows) and color-imbalanced transmission. This can be very distracting when used in environments with bright optical sources, such as the sun [19]. There are currently no compact ET systems for eyewear that offer high transparency (> 80%) across the visible, acceptable efficiencies (> 10%) for redirecting near-IR photons for imaging purposes, and strong suppression of rainbows (> 3 orders of magnitude)[5,20–23].

It is clear that a fundamentally different approach is required to realize a high-performance ET system. An optical element needs to be created that is capable of performing different, independent operations on all light waves in the VIS spectrum (let them pass completely unperturbed, independent of incident angle) and a narrow band of NIR light (to redirect it for imaging). At least in principle, linear optical elements are well-suited for the task of sorting out photons in overlapping beams by their fundamental characteristics (wavelength, polarization state or propagation direction). Physically, it is a matter of manipulating wave interference effects and the relevant mathematics is comprised of simple additions and subtractions [24]. However, in practice it can be very challenging to design a thin, ideally single-layer optical element that acts very differently on different types of waves. Only recently, new physics concepts [25] and inverse design for nanophotonics [26] have started to enable such tasks. Given the tremendous design flexibility for metasurfaces with millions of antenna elements, this technology would appear promising. However, antennas in metasurfaces display a low-quality factor (Q) and we

illustrate the need for a high-Q metasurface to create a flat optical element that can satisfy all of the demanding requirements for ET.

Figure 4A shows a photograph of our prototype ET system with a large area (4 cm^2) metasurface created on the eye-facing surface of a regular pair of glasses. A NIR-LED emitting at 870 nm illuminates an artificial eye and the metasurface redirects the scattered light from this eye toward a miniature camera attached to one of the arms. In this fashion an unperturbed, front view of the eye can be obtained. At the same time, the metasurface should afford the viewer with an unperturbed view of the outside world. To see the benefits of our metasurface, we first consider eyewear with a conventional grating composed of 30-nm-thick Cr strips and designed to redirect 10% of the NIR light. The view through such a grating is plagued by the presence of intense rainbows (See Fig. 4B). Figures 4C, D show the same scene as viewed through two of the newly-proposed guided-mode-resonance (GMR) metasurfaces. They are comprised of 7-nm-thick and 3-nm-thick poly-crystalline Si (pSi) gratings placed on a Si_3N_4 dielectric waveguide (Fig. 4E). These structures effectively suppress the rainbows and nanometer-scale changes in the thickness of the grating elements strongly impact the intensity of the rainbows. To understand the difference in behavior from a regular grating, it is of value to go back to the early modeling work on GMR structures by Hessel and Oliner [27]. They analyzed how surface-relief gratings on waveguides can couple free-space waves to quasi-guided-modes at selected resonant frequencies. The amplitude of the grating elements determines the coupling efficiency in/out of the waveguide and thus also the radiative Q for the resonance. The period of the GMR gratings has traditionally been chosen sufficiently small to suppress the generation of diffracted-orders in the super- and substrates. In this configuration, GMRs have been used to couple light into waveguides and cavities and as high-finesse optical bandpass filters [28–30]. GMRs have not yet been considered for the creation of metasurfaces capable of steering light. To achieve this goal, we need larger periodicities. Here, we propose the use of a GMR as a multifunctional metasurface for ET that is capable of passing VIS light, steering more than 10% of the NIR light to a camera, and suppressing rainbows.

The optical spectra in Figs. 4F, G quantitatively compare the distinct optical behavior of the Cr grating (Fig. 4B) and optimized GMR metasurface (Fig. 4D). The Cr grating displays a low transmissivity across the visible, which is linked to the strong absorption and scattering by the metal structures. Strong, undesired diffraction is seen across the entire visible range, consistent with Fig. 1B. This results from diffraction into second- and higher-order diffracted beams. In contrast, the 3-nm-thick GMR metasurface shows a very high transmissivity at normal incidence across the visible range (89% on average). This can be expected as the grating is at least 2 orders of magnitude thinner than the absorption depth in pSi. Moreover, the Si_3N_4 waveguide and silica cover also serve as an optimized, double-layer antireflection coating. The transmission spectrum for the GMR metasurface shows a sharp feature near 870 nm that can be attributed to a guided resonance. This resonance provides a second, indirect pathway through the structure. At the resonant

wavelength, about 40% of the light is taken out of the incident beam and redirected into four first-order diffracted beams (+1 and -1 in forward and backward directions). This can be seen in the diffraction efficiency spectrum (Fig. 1G), where the asymmetric lineshape results from the interference of the light radiating from the GMR and the directly transmitted light (i.e. the background). Based on the high diffraction efficiency seen at 870 nm, one would naturally expect to see high diffraction-efficiencies in the visible range as well. However, the GMR resonances in the VIS (at 608 nm, 496 nm, and 470 nm) display a very low diffraction-efficiency (< 0.07%), explaining the virtual absence of rainbows. The difference in behavior in the VIS and NIR lies in the spectral absorption properties of the pSi grating elements, as explained next.

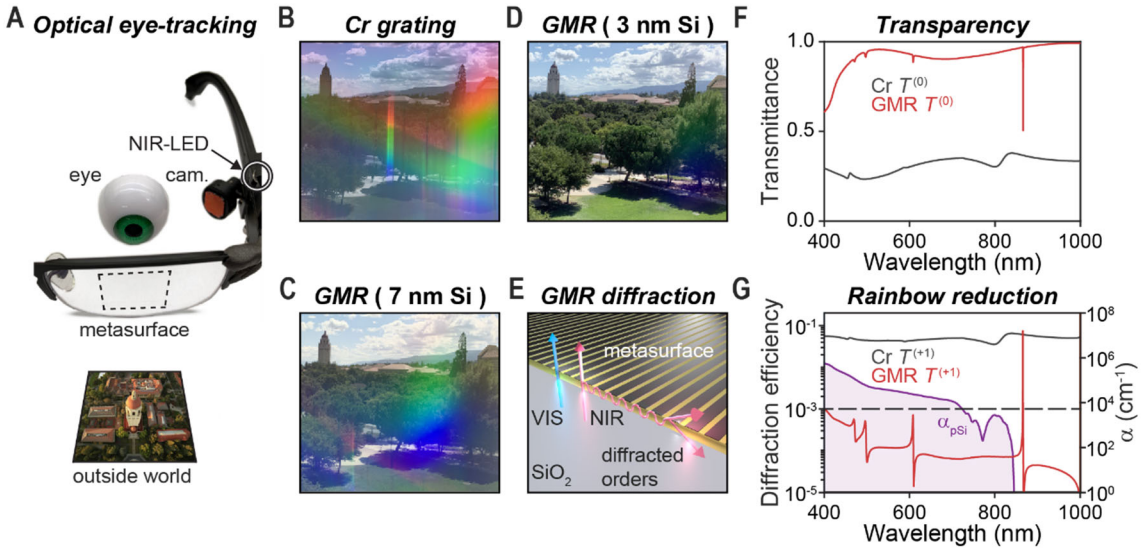

Fig. 4. Optical eye-tracking without rainbows using a high-*Q*, GMR metasurface. (**A**) Photograph of our prototype ET glasses. It illustrates how light from a NIR-LED can scatter from the eye and be redirected to a camera by a judiciously patterned surface on the glass. At the same time, the pattern should allow an unperturbed view of the outside world (Hoover tower at Stanford University). (**B**) Photograph taken through a glass surface with a 200-nm-thick Si_3N_4 anti-reflection coating patterned with a 30-nm-thick Cr grating on top showing multiple strong rainbows. Period and width of the Cr grating are 1 μm and 580 nm, respectively. (**C**) Photograph taken through a GMR metasurface with a 7-nm-thick pSi grating showing a weak rainbow. GMR metasurface is comprised of 100-nm-thick SiO_2, 7-nm-thick pSi grating, 200-nm-thick Si_3N_4 slab, and glass substrate from top to bottom. Period and width of pSi grating are 1 μm and 900 nm, respectively. (**D**) Photograph taken through a GMR metasurface with a 3-nm-thick pSi grating showing a strongly suppressed rainbow and a high, color balanced transmission. (**E**) Schematic illustrating how a GMR metasurface affords unimpeded transmission of light across the VIS and narrow-band redirection of NIR light at 870 nm into a +1 diffracted order. (**F**) Simulated zeroth-order transmittance spectra of the Cr grating and optimized GMR metasurface under normally incident planewave illumination. The polarization direction is in parallel to the grooves of the grating (TE). (**G**) Simulated diffraction efficiency into the +1 diffracted-order transmission for the 30-nm-thick Cr grating and the optimized GMR metasurface under normally incident TE polarized planewave incidence. Both structures reach ~10% efficiency at the target wavelength of 870 nm. The

horizontal dashed line indicates a 0.1% upper limit for visible light diffraction to avoid perceptible rainbows. The shaded region shows the absorption coefficient of grown pSi.

The flow of light through the GMR metasurface is controlled by the relative magnitudes of the scattering and absorption efficiencies of the grating elements. These can be engineered through a choice of the material and geometry for these elements. To obtain very different behavior in the VIS and NIR, we chose pSi as its absorption depth changes by several orders of magnitude between these spectral ranges. Figure 5A illustrates the power flow for incident planewaves in the VIS and NIR. In both spectral ranges, light can couple to the GMR by picking up the second-order grating momentum ($=4\pi/p$), where p is the grating period. The dispersion diagram in Fig. 5B shows this process for 870 nm transverse electric (TE) polarized light. Subsequent radiative decay from the GMR into the first diffracted-order then produces the desired steered beam for imaging. One might expect the coupling into the guided mode by a mere 3-nm-thick grating to be very ineffective. However, the decoupling by such a thin grating is also very weak and this enables a resonance with a high Q of 8700 at $\lambda = 870$ nm. This Q is radiation-limited as the pSi shows weak materials absorption at this wavelength. As such, the light is trapped inside the Si_3N_4 slab waveguide for many optical cycles ($=Q/2\pi$) and a strong buildup of the internal fields in the GMR ($|E|^2/|E_{inc}|^2 \approx 2500$) is observed. In turn, the large internal fields enable high diffraction efficiencies of 11.1% for the first-order reflected beams, consistent with temporal coupled mode theory (CMT). The diffraction is clearly noticeable from the checkerboard pattern of nodes in the electric field intensity profile in Fig. 5C. In contrast, in the visible part of the spectrum the pSi materials absorption is significantly stronger. As a result, the quality factor is absorption dominated and the field build up in the guided resonance results in a strongly enhanced light absorption. In this wavelength range, the power in the GMR dissipates before it is decoupled to free-space. Physically, the enhanced absorption results from a long interaction length with the absorbing pSi grating elements as the light is guided along the nitride waveguide. This results in a low first-order diffraction efficiency (< 0.1%) results, as confirmed by CMT and a power flow analysis. For the directly transmitted light there is no noticeable energy storage and we find that the essentially single-pass transmission through the 3-nm-thick pSi grating provides a very high (close to 90%) transmittance. At this point it is worth noting that the Cr strips in the conventional grating only support low-Q scattering resonances. Such resonances do not afford the significant field build up that is required to achieve independent control over the power flow paths in the VIS and NIR.

There are several trade-offs in the metasurface design. Thicker pSi gratings elements can more effectively scatter than absorb light and can thus offer more intense first-order diffracted beams for ET. Figure 5D shows the simulated dependence of the diffraction efficiency for the TE-polarized GMR near 870 nm into the first-order reflected beam used for ET. Here, we take a representative refractive index of pSi ($=3.7+0.005i$) in this spectral regime[31]. Despite the very weak materials absorption of pSi at this wavelength, the absorption ends up dominating the total quality factor for very thin strips (~1 nm). The peak diffraction efficiency then increases as a function of the grating height and saturates

as the scattering by the strips starts dominating the absorption. At a 2 nm grating height, the diffraction efficiency already exceeds 4%. Figure 5E summarizes the diffraction efficiency into the unwanted, first-order transmitted beam for the TE-polarized GMR in the visible (near 605 nm). In this spectral region, the pSi is significantly more absorptive ($n = 4.0 + 0.1i$) and the peak diffraction efficiency is decreased by 2 orders of magnitude as compared to the NIR. The peak diffraction efficiency falls below 0.1% for grating heights smaller than 4 nm, which we therefore set as the maximally acceptable grating height. Combined, these requirements locate the optimum grating height around 3 nm. Finally, such a grating height is also thin enough to fulfill the >80% transmittance requirement (See Fig. 5F).

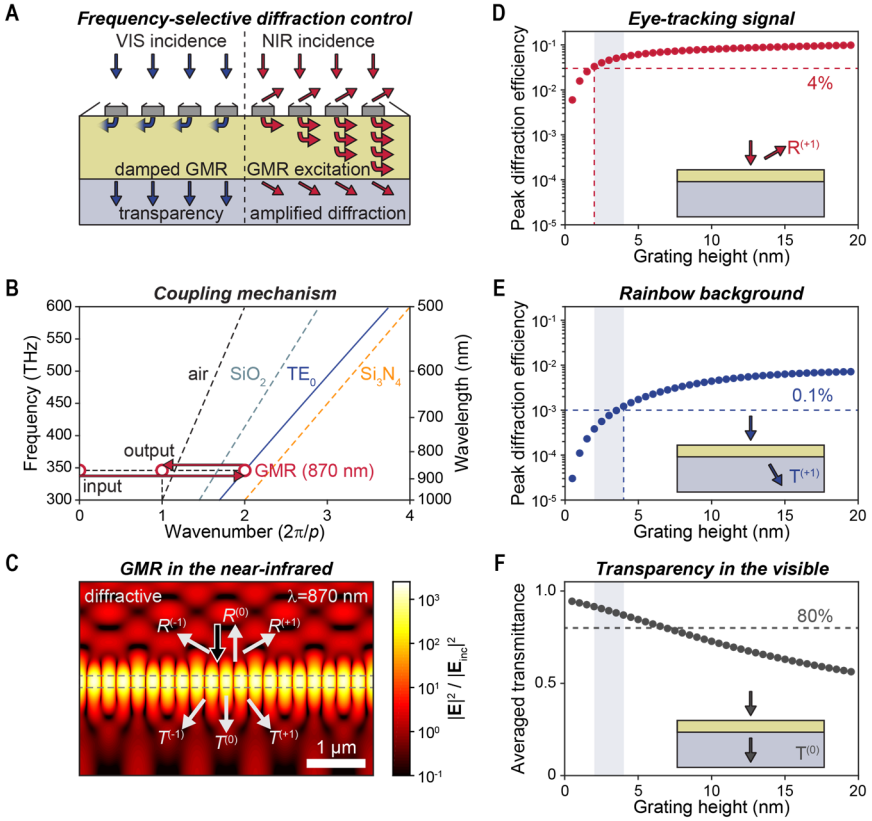

Fig. 5. Resonant diffraction mechanism of GMR metasurface. (**A**) Schematic showing the optical power flow of input planewaves in the VIS and NIR into the transmitted and diffracted channels as mediated by the GMR metasurface. (**B**) Dispersion relation for the TE_0 mode supported by the Si_3N_4 waveguide. The black, cyan, and yellow dashed curves are the light lines for air, SiO_2, and Si_3N_4, respectively. The horizontal red arrow to the right indicates the excitation of the GMR by a normally-incident planewave. The red arrow to the left designates the decoupling from the TE_0 waveguide mode into the 1st diffracted order at grazing exit (i.e. close to the air light line). (**C**) Electric field intensity profile of the TE GMR excited on resonance at 870 nm. The black arrow indicates the incident planewave and the 6 white arrows represent the output diffractive orders (including zeroth-orders). (**D**) Resonant peak diffraction efficiency at the TE GMR in the NIR as a function of the Si grating height. All structural parameters except the grating height are fixed. (**E**) Resonant peak diffraction efficiency of TE GMR in the VIS. (**F**) Averaged transmittance of the GMR structure across the visible range (400 - 700 nm) for TE polarization. The dashed horizontal line shows a minimum required transmittance for a practical device.

The analysis above indicates that we need atomic-scale control over the Si grating thickness across the 4 cm^2 area of the metasurface. The scanning electron microscopy (SEM) image in Fig. 6 shows how we can achieve such high accuracy by adopting standard photolithography and Si-compatible processes. A pSi deposition followed by a slow thermal Si oxidation process enables sub-nanometer control over the pSi layer height. The cross-section of the grating pattern shows a 30-nm-deep over-etching of the pSi layer into the Si_3N_4 slab (Fig. 6B). The over-etching increases the radiative decay rate compared to that for non-over-etched case. Cross-polarized transmission measurements remove the direct, non-resonant transmission channel for the metasurface and clearly show the sharp resonance peaks from the GMRs (Fig. 6C). The measured quality factor (Q = 540) is lower than in the simulation (Q = 1400), which we attribute to the increased radiative decay rate by the fabrication imperfection (i.e. grating width).

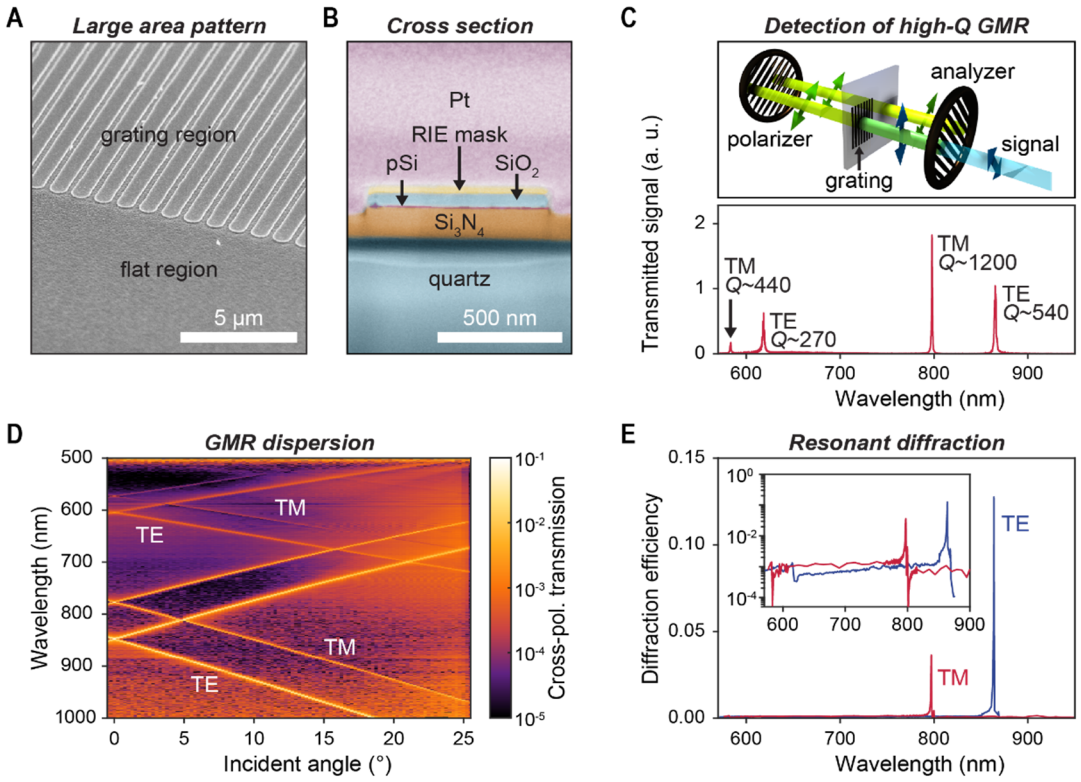

Fig. 6. Experimental realization of the GMR metasurface. (**A**) SEM image of the fabricated GMR metasurface. (**B**) False-colored SEM image of a focused-ion beam cross section of a single unit cell. (**C**) Cross-polarized transmittance spectrum of the metasurface at normal incidence illumination. The top panel depicts the cross-polarized transmission measurement setup. (**D**) Measured optical dispersion for the GMR metasurface as obtained from the cross-polarized transmittance spectra and as a function of the incident angle. (**E**) Measured diffraction efficiency (first-order reflection) of the metasurface. The inset shows the same data plotted on a logarithmic scale.

Using a home-built angle-resolved confocal spectroscopy setup, we characterize the optical dispersion (Fig. 6D) as well as the power efficiency of the resonant diffraction (Fig. 6E) by the GMR metasurface. Figure 6E shows the measured peak diffraction efficiency spectra for both TE and TM polarizations. The measured data agrees well with those of the corresponding simulations. We find that the TE GMR at 864 nm delivers a 12.8% diffraction efficiency. The slightly larger peak diffraction efficiency compared to the simulation (11.1%) is attributed to a small deviation in the width of the pSi grating elements from the original design. This mode provides an excellent platform to redirect normally-incident NIR light from the eyes into the desired direction (60°), where the ET camera is positioned. The diffraction in the visible spectrum is suppressed to 0.07% on average while maintaining high degree of zeroth-order transmission (> 85%).

Figure 7A shows a front view of the prototype ET glasses where the location of the GMR metasurface outlined. This front view of the eye is also seen by the camera after a redirection by the metasurface. We develop a basic ray-tracing approach to describe the image formation by the metasurface. It is used to transform a collection of points in the object space to a set of stigmatic points in a virtual image as depicted in Fig. 7B. The stigmatic points can be located by considering the path of two rays originating from a single point on the eye (e.g. f). The diffracted rays can be extended back from the metasurface to find the stigmatic points (e.g. f'). From such an analysis, it is clear how the camera can capture the front view of the eye through a diffracted order. It further illustrates how the eye's image is compressed along the z-direction and pulled towards the metasurface. This action enables us to track large lateral motions of the pupil and spatially resolve features of the eye, no matter how far the eye is located from the metasurface. A possible concern with imaging through a diffractive order is the spatial resolution along the x-direction. The high-Q of the GMR metasurface limits the range of angles that can effectively couple to the guided mode and thus can be used for imaging. A detailed analysis shows that the spatial resolution is determined by the numerical aperture of the system as $d = \lambda_r/2\text{NA} = \lambda_r Q/2\pi n_g$, where λ_r and n_g are the wavelength and group index of the relevant guided mode. Plugging in the experimentally obtained values of λ_r (= 864 nm), Q (= 540), and n_g (2.04) we find a spatial resolution of ~ 40 μm. Figure 7C shows the different spatial resolution in the x- and y-direction for 1.12 mm wide bars. This spatial resolution is sufficient to image the key features of the eye even at large angle rotations, as shown in Fig. 7D. Higher spatial resolutions can be achieved using a lower Q metasurface at the cost of increased rainbows.

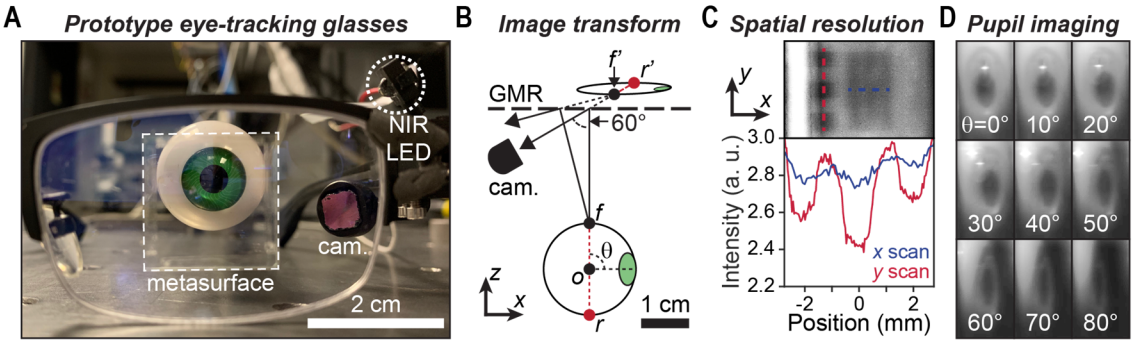

Fig. 7. Optical eye-tracking prototype demonstration. (**A**) Front image of the ET prototype showing the transparent metasurface in front of the eye. (**B**) Schematic showing how the eye is imaged through a diffracted order of the metasurface. A ray-optics picture can be used to explain how the eye's image is compressed and pulled towards the metasurface. This action affords facile capture of large eye rotations. (**C**) Imaging of vertical and horizontal lines from a USAF calibration chart, shows that a different spatial resolution is achieved in the *x*- and *y*-directions. The top panel shows the diffractive image of USAF lines with 1.12 mm width. The bottom panel shows the cross section intensity along the horizontal (blue line) and vertical (red line) directions, as integrated over a 1.2 mm band (30 lines). (**D**) Optical images taken from the eye with the ET camera. A wide range of rotation angles (up to $\theta = 80°$) can be imaged and the spatial resolution is sufficient to quantify the size and motion of the sclera, iris, and pupil.

II.4. Conclusions and future directions for high-Q metasurfaces

From a practical perspective, the created high-Q metasurfaces offer a high-performance flat-optics platform that affords facile tracking of the eye's motion. From a fundamental perspective, we have demonstrated that single-layer, high-Q metasurfaces can perform independent actions on overlapping beams of visible and near-infrared light. A feat that has been elusive for metasurfaces constructed from low-Q antennas and that may find applications beyond ET. We are currently exploring the possibility to develop optical beam combiners for communication and projection technology.

II.5. Atomically-thin metasurfaces function and dynamic lenses

Ever since the development of diffractive optical elements in the 1970s, researchers have uncovered increasingly sophisticated, fundamental optics principles by which bulky optical elements can be replaced by thin, lightweight counterparts[32]. This has recently culminated in a worldwide activity aimed at creating nanophotonic metasurfaces, essentially flat optics composed of dense arrays of metal or semiconductor nanostructures[5,33]. Such structures facilitate effective control over the local light scattering phase and amplitude by employing plasmonic[34] or Mie resonances[35]. These two types of resonances have been instrumental in realising small-form-factor optics delivering multi-functionality[6,7], very high-numerical apertures[8,9], minimal aberrations[10–12], non-linear optics[36,37], and control over the light field[14,38]. Despite these impressive advances, metasurface functions have largely remained static. For emerging applications, such as light detection and ranging (LIDAR), dynamic

holography, computational imaging, and sensing[39,40], it would be highly desirable to find ways to electrically-activate metasurfaces and achieve dynamic control.

Whereas the importance of plasmonic and Mie resonances in metasurface design cannot be overstated, their use in active metadevices can also prove limiting as they tend to offer only weak electrical tunability. This finds its origin in the limited magnitude of most electroabsorption and electrorefraction effects in metals and semiconductors. It is thus worth considering what other resonances can be utilized in realising electrically-tuneable flat optics. From decades of research on optical modulation, it is clear that the strongest, high-speed modulation of materials optical properties is achieved by manipulating excitons, electron-hole pairs in semiconductors bound by the Coulomb force[41]. Their resonant excitation can give rise to sharply-peaked absorption features, just below the bandgap of a semiconductor. The associated absorption coefficients can reach levels of 1000 cm^{-1}. In the larger (~100 nm) Mie-resonant semiconductor nanostructures used in metasurfaces, the optical materials properties are essentially bulk-like and the exciton binding energy tends to be small (5 - 10 meV). As a result, the excitonic features are absent at room temperature. In contrast, excitons dominate the near-edge optical properties of 2-dimensional (2D) semiconductors, such as the monolayer transition metal dichalcogenides (TMDCs). The reduced screening in these quantum materials leads to binding energies of hundreds of meV and consequently excitons can exist even at room temperature[42,43]. Exciton resonances can also effectively be tuned over several 100 meV with changes in the materials composition, environmental index[44–46], electric/magnetic fields[44,47], and strain[48,49]. The suppression of exciton states through carrier injection[50–52] can have an even stronger impact on the material optical properties. Based on recent measurements showing near-unity reflectivity from monolayers of $MoSe_2$[53–55], it is also clear that the interaction with a single layer can be extremely strong.

These findings raise the intriguing question whether excitonic resonances can be harnessed to realise electrically-tuneable and atomically-thin metasurface components. Materials with excitonic resonances have already been placed near plasmonic and Mie resonators with the goal of tuning them through strong coupling[56,57]. A variety of passive optical elements has also been realised by patterning multilayer 2D TMDCs[58,59], multilayer graphene[60], and 200-nm thick graphene oxide[61], and even small-area, monolayer TMDCs[62]. However, the critical role excitons can play in optical wavefront manipulation has not been yet been elucidated and a demonstration of active modulation of atomically-thin optical elements has therefore remained elusive.

Here, we demonstrate large-area, actively-tuneable and atomically-thin optical elements by carving them directly out of a monolayer of WS_2. This material displays a strong excitonic resonance in the visible spectral range. Counter to the usual approach of engineering the size and shape of geometrically-resonant antennas, the design of metasurfaces made from 2D excitonic materials relies on identifying, engineering and modifying this materials resonance. Furthermore, in optimizing the spatial arrangement of

2D materials to achieve specific optical functions, it is important to realise that resonant, tuneable light-matter interaction is naturally obtained wherever the material is located. These notions open entirely new design strategies for highly-tuneable flat optics.

Figure 8a illustrates an atomically-thin zone-plate lens whose properties can be controlled by electrical gating with an ionic liquid. It is 1 mm in diameter and features a series of 202 concentric rings that are patterned into a monolayer of WS_2 grown by chemical vapor deposition on sapphire. The design of the ring diameter and spacing is conceptually similar to that of a conventional zone plate and aims to achieve constructive interference of the diffracted light from the WS_2 rings into a sharp focus. Figure 8b presents the centre part of the zone plate lens. To facilitate dynamic electrical control over the lens properties, we found that it is beneficial to transfer a large-area graphene monolayer (Gr) on top of the WS_2 as a transparent electrode. The graphene facilitates enhanced DC surface conductivity and warrants uniform gating of the WS_2. It also serves as a protective layer for the WS_2 in the electrochemical gating experiments and enhances long-term stability. It is known that monolayer graphene does not fully screen gate-induced electric fields, allowing effective doping of the underlying WS_2[63]. A total of 8 gold radial finger-electrodes are applied to bias the lenses. Finally, we place an optically-transparent electrochemical cell filled with ionic liquid (DEME-TFSI) on top (see Fig 8c).

When the lens is bottom-illuminated with 620 nm light, we can use confocal scanning microscopy to characterize the shape and intensity of the focused beam. A clear focal spot is observed (Fig. 8b inset) behind the lens with a characteristic flat-top beam profile that is well-described by a super-Gaussian line shape64 with a full-width at half-maximum of 6.7 μm. The spot size and shape result from the experimental illumination conditions. The measured focal length is slightly shorter than the free-space design of 2 mm due to the presence of the electrochemical cell (Fig. 8d).

To highlight the important role exciton resonances can play in the operation of the flat lens, it is of value to view the rings of WS2 as sources of scattered field, driven by an incident plane wave. The locally generated scattered fields are proportional to the polarization P = ε0□Ei of the WS2 material, where ε0 is the permittivity of free space, □ the complex electric susceptibility, and Ei is the local driving electric field. The spectral behaviour of □ is thus encoded into the spectral dependence of the amplitude and phase of the scattered fields. The strongest scattering is therefore expected near the exciton resonance where the magnitude of □ is largest and we explore this situation first.

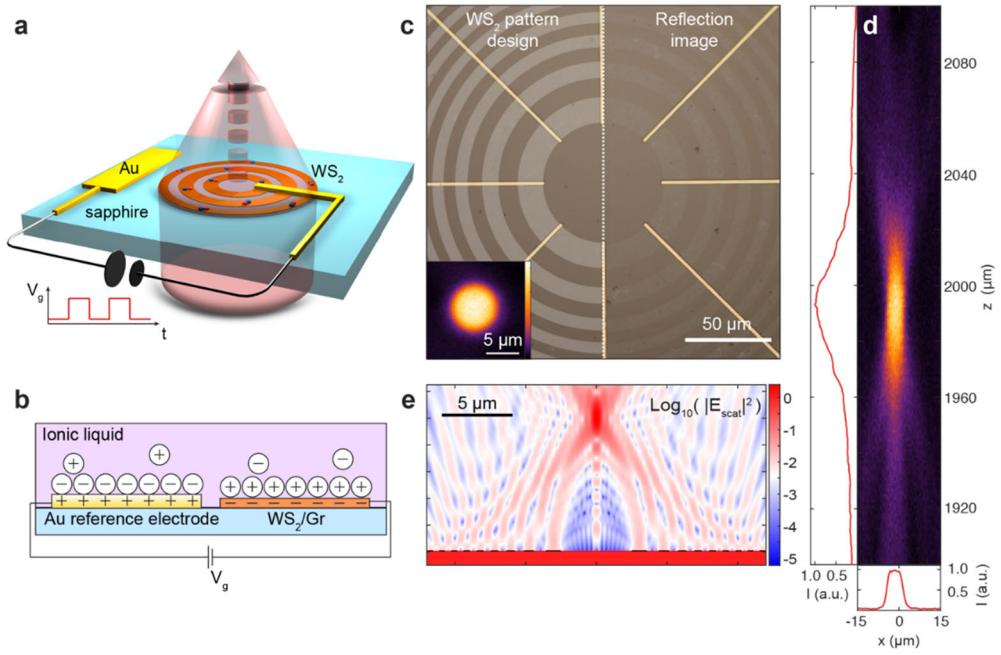

Fig. 8 | Atomically-thin and tuneable flat lenses. a, Schematic of the proposed WS_2 zone plate lens in an electrochemical cell. Time-varying ion-liquid gate voltages result in a modulation of the focusing efficiency by quenching exciton resonances. **b**, Optical microscope image of the centre of a fabricated lens (right) and the designed WS_2 pattern overlaid (left, light shaded regions). Inset: *xy*-scan of the focus formed approximately 2 mm above the patterned surface (λ = 620nm). **c**, Photograph of the mm-scale lenses inside an electrochemical cell for ion-liquid gating. The cell is mounted and wire bonded to a custom-made printed-circuit board that enables optical transmission experiments. **d**, *xz*-scan of the focused beam (λ = 620 nm). Crosscuts of the normalized intensity along the *z*-axis of the focused beam and *x*-axis (for z = 1993 μm) are also shown in arbitrary units (a.u.). **e**, Scattered field intensity (λ = 620 nm) behind a 20-μm-diameter zone plate lens with a focal length f = 10 μm on sapphire (Log_{10} colour scale).

Figure 8e shows a scattered field simulation that illustrates the focusing action of a 20-μm-diameter WS_2 zone plate lens illuminated at the exciton resonance wavelength (λ = 620 nm). Using room temperature literature values for exfoliated WS_2[65] for χ we find a focusing efficiency of 0.08 %. Significantly higher focusing efficiencies could be reached with higher-quality exfoliated materials and at low temperatures for which the exciton linewidth is noticeably reduced[53–55]. Even at these low diffraction efficiencies these lenses can have important applications in free-space optical beam tapping and sensing[66]. Whereas the current lens is virtually invisible to the human eye for non-resonant wavelengths, it can capture important information from its surroundings and the intensity in the focus well-exceeds the intensity of the incident plane wave (by a factor 2.75) as the light is concentrated by the ratio of the lens area to the focal spot size of about 10^3. This factor is

for the simulated 20-µm-diameter lens and significantly larger concentration is achieved with our mm-sized, fabricated lenses.

The spectral dependence of the focusing efficiency is intrinsically linked to the complex material susceptibility χ of the WS_2 monolayer. Using literature values for χ (ref. 65), we find that the susceptibility near the A and B exciton resonances appears as loops in the complex plane with a radii proportional to the oscillator strength of each resonance (Fig. 9a). As a result, the resonances not only give rise to a strong oscillation in the magnitude of χ, but also a notable change in phase angle up to $\sim 0.4\pi$ around $\lambda = 617$ nm (Fig. 9b). In the absence of the direct substrate transmission, the scattered light intensity in the focus of the 20-µm-diameter WS_2 zone plate lens (as obtained from Fig. 8e) also shows an asymmetric line shape that is governed by the WS_2 material susceptibility squared (Fig. 9c). Experimentally, the scattered fields cannot be isolated, and the spectral line shape results in general from interference with the direct substrate transmission. However, by collecting the weakly scattered light from a large area (1 mm diameter), the focal intensity of our experimental zone plates is high and largely determined by the scattered fields from the WS_2 material.

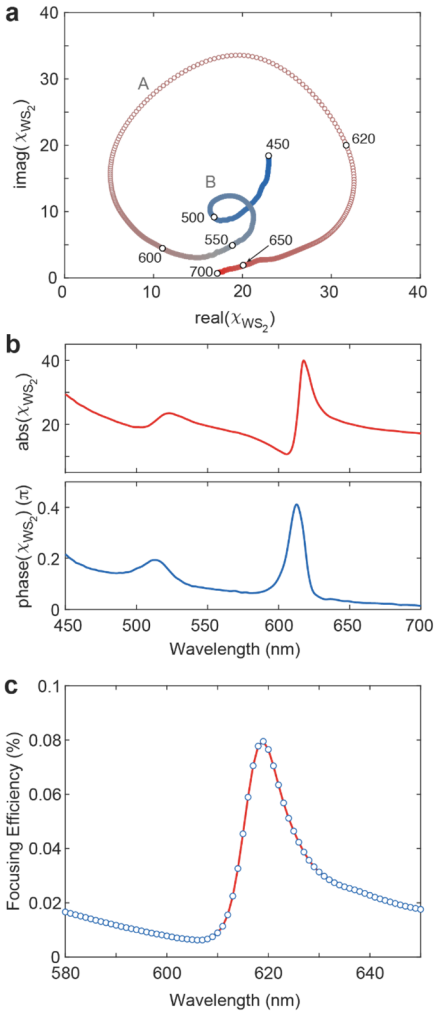

Fig..9 | Material susceptibility and focusing efficiency. a, Phasor plot of the complex susceptibility of the WS_2. The white dots and numbers indicate the corresponding wavelengths. "A" and "B" refer to the exciton resonances. **b**, Absolute value (top) and phase angle (bottom) of the material susceptibility. **c**, Simulated focusing efficiency spectrum of the scattered light for the 20 µm diameter zone plate lens shown in Fig. 1e.

The possibility to modulate the focusing efficiency of our lens stems results from our ability to alter the exciton resonances of the WS_2 material via electrical gating. We first analyse the induced reflectivity changes from a simple square 20×20 μm^2 isolated patch of monolayer WS_2 (inset to Fig. 10a) as a function of applied gate voltage. As expected, the reflection spectrum is dominated by the "A" and "B" excitons at λ = 520 nm and λ = 625 nm, respectively. Note that the line width of the main reflection peak (~75 meV) is notably larger than reported for exfoliated flakes[65], quite common for lower quality, large-area CVD-grown WS_2 monolayers. The main excitonic reflection peak is completely suppressed and a small, red-shifted peak at λ = 655 nm is observed when a 3 V gate bias is applied to induce n-type doping. The suppression and red-shift of the A-exciton result from a screening of the electron-hole interaction due to the increased electron density and an interconversion to negatively-charged exciton states (A^- trions)[52,67]. A similarly strong suppression is observed for the "B" exciton located at λ = 520 nm. The observed complete removal of the excitonic resonances is known to produce one of the largest possible changes in the susceptibility[41]. The exciton suppression is also fully reversible and highly reproducible (Fig. 10b). These observations highlight the benefits of excitonic resonances over plasmonic and Mie-type resonances, which are much harder to tune or quench.

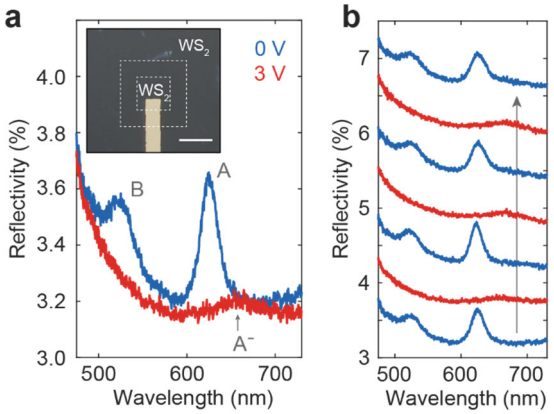

Fig. 10 | Exciton manipulation through ion-liquid gating. a, Reflectivity spectra of a 20×20 μm^2 isolated patch of WS_2 for V_g = 0 V (blue) and gated at V_g = 3 V (*n*-doping, red). Inset: optical microscope image of the patch device. The WS_2 in between the dashed lines is removed, isolating the inner WS_2 area. Scale bar: 20 μm. **b**, Reflectivity spectra while cycling between the neutral (blue) and doped state (red) showing high reproducibility. Sequentially obtained spectra are offset for clarity, as indicated by the gray arrow.

Next, we will capitalize on the large tunability of the exciton resonances to modulate the intensity in the focal spot of a lens. We experimentally measure the power in the focus as a function of wavelength and normalize to the power incident on the zone plate lens to determine the focusing efficiency spectrum (see Methods for procedure). A clear asymmetric line shape is observed for the pristine zone plate lens (Fig. 11a, red), closely matching the calculated response in Fig. 9c which omitted the directly transmitted light.

This correspondence is a clear indication that the focused excitonic light scattering dominates the direct substrate transmission. Next, we apply a 3 V bias to the WS_2/Gr heterostructure to suppress the exciton resonance. The asymmetric excitonic line is fully suppressed (Fig. 11a, blue) and a flat non-resonant efficiency spectrum is clearly observed. Note that slight over etching into the substrate during the sample fabrication gives rise to non-resonant background focusing. Finally, we use the reversible switching of the exciton resonance to restore the neutral resonant state (Fig. 11a, grey). The distinctive asymmetric resonant line shape is reproduced, with an enhanced amplitude that corresponds to an increase in oscillator strength and reduction in exciton line width. This is consistent with observations of line width narrowing in reflection measurements on our patch devices (like Fig. 11a) upon the first gating cycle. We attribute this effect to the passivation of positively-charged intrinsic and fabrication-induced defects during the first gating cycle. We note that the measured focusing efficiency is relatively low (<0.1 %) and is primarily limited by the relatively low material quality of the commercial WS_2. Recent experiments on small flakes of $MoSe_2$ have demonstrated that high-quality encapsulated monolayers can achieve an optical reflectance of ~80% [53–55]. Improvements in the large-area growth of high-quality monolayer TMDCs will therefore strongly enhance the focusing efficiencies.

Using room-temperature large-area active manipulation of the exciton resonance, we demonstrate dynamic light intensity modulation in the focus of the 2D material zone plate lens (Fig. 11b). Reproducible switching between the exciton-dominated (V_g = 0 V) and the exciton-quenched state (V_g = 3 V) enables active control over excitonic light scattering amplitude (Fig. 11b). The asymmetric exciton resonance line shape in the focusing efficiency gives rise to decreased (λ = 605 nm) or increased (λ = 625 nm) intensity in the focus compared to the non-resonant state. For λ = 615 nm the efficiency curves intersect (Fig. 11a) however, which results in no observable contrast (Fig. 11b). The maximum modulation depth observed is ~33% for λ = 625 nm, despite the single-pass interaction of light with the atomically-thin structure. In our current sample, the modulation depth is limited by non-resonant background focusing as a result of the gently over-etched pattern. The typical device response time is characterized from accumulated time traces (5 ms resolution) of the focal intensity for λ = 625 nm. The rise and fall time are measured to be 39 ± 3 ms and 16 ± 1 ms, respectively. The response time and asymmetry are a result of the ion-transport limited complex formation and disassembly of the ionic-liquid electrical double layer[68]. Implementing solid-state gating schemes rather than ion-liquid gating would increase the device response time by orders of magnitude and is merely limited by fabrication challenges.

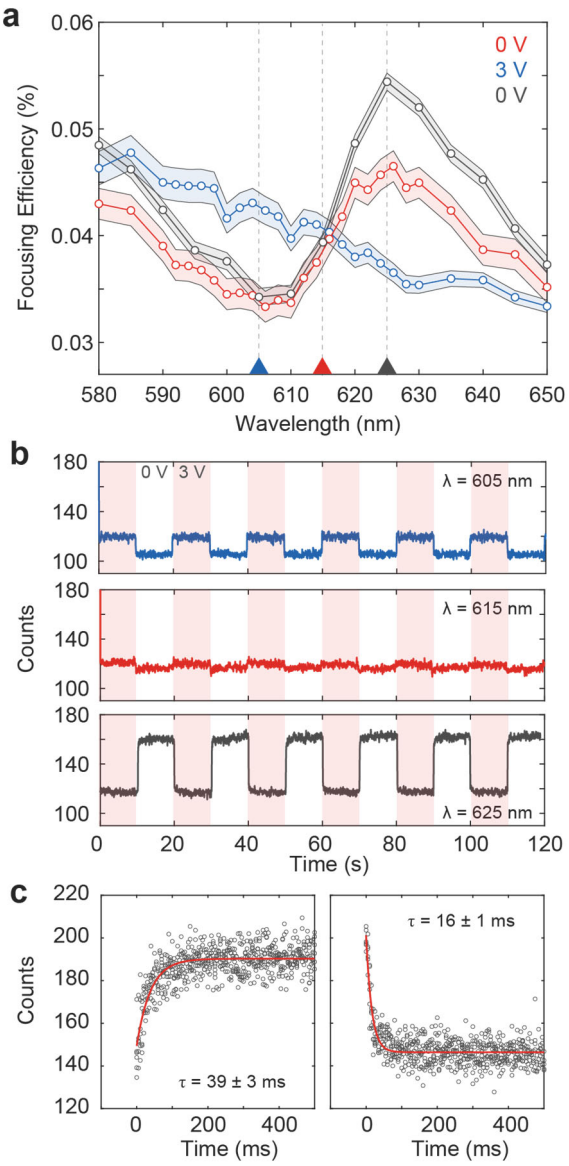

Fig. 11. Exciton modulation of the intensity in the focus. a, Focusing efficiency spectrum of the zone plate lens in pristine (red, V_g = 0 V), gated (blue, V_g = 3 V), and restored state (gray, V_g = 0 V). The shaded area indicates the error bar corresponding to one standard deviation. The triangles at the bottom axis and dashed lines indicate the wavelengths used for (b). **b**, Intensity in the focus as a function of time for λ = 605 nm (blue, top), for λ = 615 nm (red, middle), and for λ = 625 nm (gray, bottom) while V_g is cycled between 0 V (white background) and 3 V (red background). **c**, Time trace of rise (left) and fall (right) of the focal intensity for λ = 625 nm. The corresponding rise and fall times obtained from a fit (red) are also shown.

II.6. Conclusions on the work on creating atomically-thin, dynamic optical elements

The presented results on atomically thin lenses demonstrate the important role of excitonic material resonances can play in the operation atomically-thin optical elements. More advanced gating schemes with local and interleaved gating electrodes will enable excitonic optical devices with more complex tuneable functionalities including tuneable focal lengths or beam steering. The highly-tuneable nature of these excitonic material resonances opens an entirely approach for the design of dynamic flat optics and metasurfaces with applications in free-space beam tapping, wavefront manipulation, spectral polarimetry, and augmented/virtual reality.

II.7 **References**

1. Yi, S. *et al.* Subwavelength angle-sensing photodetectors inspired by directional hearing in small animals. *Nat. Nanotechnol.* **13**, 1143–1147 (2018).
2. Lin, D. *et al.* Polarization-independent metasurface lens employing the Pancharatnam-Berry phase. *Opt. Express* **26**, 24835–24842 (2018).
3. Van De Groep, J. & Brongersma, M. L. Metasurface Mirrors for External Control of Mie Resonances. *Nano Lett.* **18**, 3857–3864 (2018).
4. Chen, H. T., Taylor, A. J. & Yu, N. A review of metasurfaces: Physics and applications. *Reports on Progress in Physics* **79**, 076401 (2016).
5. Khorasaninejad, M. & Capasso, F. Metalenses: Versatile multifunctional photonic components. *Science* **358**, eaam8100 (2017).
6. Kamali, S. M. *et al.* Angle-multiplexed metasurfaces: Encoding independent wavefronts in a single metasurface under different illumination angles. *Phys. Rev. X* **7**, 041056 (2017).
7. Maguid, E. *et al.* Multifunctional interleaved geometric-phase dielectric metasurfaces. *Light Sci. Appl.* **6**, e17027-7 (2017).
8. Paniagua-Domínguez, R. *et al.* A metalens with a near-unity numerical aperture. *Nano Lett.* **18**, 2124–2132 (2018).
9. Liang, H. *et al.* Ultrahigh numerical aperture metalens at visible wavelengths. *Nano Lett.* **18**, 4460–4466 (2018).
10. Khorasaninejad, M. *et al.* Metalenses at visible wavelengths: Diffraction-limited focusing and subwavelength resolution imaging. *Science* **352**, 1190–1194 (2016).
11. Shrestha, S., Overvig, A. C., Lu, M., Stein, A. & Yu, N. Broadband achromatic dielectric metalenses. *Light Sci. Appl.* **7**, 85 (2018).
12. Wang, S. *et al.* A broadband achromatic metalens in the visible. *Nat. Nanotechnol.* **13**, 227–232 (2018).
13. Lin, R. J. *et al.* Achromatic metalens array for full-colour light-field imaging. *Nature Nanotechnology* **14**, 227–231 (2019).
14. Holsteen, A. L., Lin, D., Kauvar, I., Wetzstein, G. & Brongersma, M. L. A light-field metasurface for high-resolution single-particle tracking. *Nano Lett.* **19**, 2267–2271 (2019).
15. Duchowski, A. *Eye tracking methodology: Theory and practice*. *Eye Tracking Methodology: Theory and Practice* (Springer, 2009).
16. Cognolato, M., Atzori, M. & Müller, H. Head-mounted eye gaze tracking devices:

An overview of modern devices and recent advances. *J. Rehabil. Assist. Technol. Eng.* **5**, 205566831877399 (2018).
17. Richardson, D. & Spivey, M. Eye Tracking: Characteristics and Methods. *Encycl. Biomater. Biomed. Eng. Second Ed. - Four Vol. Set* 1028–1032 (2008). doi:10.1201/b18990-101
18. Yarbus, A. L. *Eye Movements During Change of Stationary Points of Fixation in Space*. *Eye Movements and Vision* (Plenum Press, 1967).
19. Mirza, K. & Sarayeddine, K. Key challenges to affordable see through wearable displays: the missing link for mobilearmass deployment. *Optivent SA, Rennes, Fr.* **33**, 1–6 (2012).
20. Liu, C., Pazzucconi, B., Liu, J., Liu, L. & Yao, X. A holographic waveguide based eye tracking device. *J. Mod. Opt.* **66**, 1311–1317 (2019).
21. Lee, G. Y. *et al.* Metasurface eyepiece for augmented reality. *Nat. Commun.* **9**, 4562 (2018).
22. Sanjeev, V. *et al.* A broadband achromatic metalens for focusing and imaging in the visible. *Nat. Nanotechnol.* **13**, 220–226 (2017).
23. Li, Z. *et al.* Full-space Cloud of Random Points with a Scrambling Metasurface. *Light Sci. Appl.* **7**, (2018).
24. Miller, D. A. B. Sorting out light. *Science* **347**, 1423–1424 (2015).
25. Shen, Y. *et al.* Optical broadband angular selectivity. *Sci. (New York, N.Y.* **343**, 1499–1501 (2014).
26. Molesky, S. *et al.* Inverse design in nanophotonics. *Nature Photonics* **12**, 659–670 (2018).
27. Hessel, A. & Oliner, A. A. A New Theory of Wood's Anomalies on Optical Gratings. *Appl. Opt.* **4**, 1275 (1965).
28. Wang, S. S. & Magnusson, R. Theory and applications of guided-mode resonance filters. *Appl. Opt.* **32**, 2606 (2009).
29. Magnusson, R., Shin, D. & Liu, Z. S. Guided-mode resonance Brewster filter. *Opt. Lett.* **23**, 612 (2008).
30. Wang, S. S., Moharam, M. G., Magnusson, R. & Bagby, J. S. Guided-mode resonances in planar dielectric-layer diffraction gratings. *J. Opt. Soc. Am. A* **7**, 1470 (1990).
31. Aspnes, D. E. & Studna, A. A. Dielectric functions and optical parameters of Si, Ge, GaP, GaAs, GaSb, InP, InAs, and InSb from 1.5 to 6.0 eV. *Phys. Rev. B* **27**, 985 (1983).
32. Lalanne, P. & Chavel, P. Metalenses at visible wavelengths: past, present, perspectives. *Laser Photonics Rev.* **11**, (2017).
33. Chen, H. T., Taylor, A. J. & Yu, N. A review of metasurfaces: Physics and applications. *Reports Prog. Phys.* **79**, 076401 (2016).
34. Yu, N. *et al.* Light propagation with phase discontinuities: generalized laws of reflection and refraction. *Science* **334**, 333–337 (2011).
35. Lin, D., Fan, P., Hasman, E. & Brongersma, M. L. Dielectric gradient metasurface optical elements. *Science* **345**, 298–302 (2014).
36. Li, G., Zhang, S. & Zentgraf, T. Nonlinear photonic metasurfaces. *Nat. Rev. Mater.* **2**, 17010 (2017).
37. Krasnok, A., Tymchenko, M. & Alù, A. Nonlinear metasurfaces: a paradigm shift

in nonlinear optics. *Mater. Today* **21**, 8–21 (2018).
38. Lin, R. J. *et al.* Achromatic metalens array for full-colour light-field imaging. *Nat. Nanotechnol.* **14**, 227–231 (2019).
39. Schwarz, B. Lidar: Mapping the world in 3D. *Nat. Photonics* **4**, 429–430 (2010).
40. Jung, I. W. *et al.* 2-D MEMS scanner for handheld multispectral confocal microscopes. in *2012 International Conference on Optical MEMS and Nanophotonics* 238–239 (2012). doi:10.1109/OMEMS.2012.6318891
41. Miller, D. A. B. Attojoule Optoelectronics for Low-Energy Information Processing and Communications. *J. Light. Technol.* **35**, 346–396 (2017).
42. Mak, K. F., Lee, C., Hone, J., Shan, J. & Heinz, T. F. Atomically thin MoS_2: A new direct-gap semiconductor. *Phys. Rev. Lett.* **105**, 136805 (2010).
43. Cao, L. Two-dimensional transition-metal dichalcogenide materials: Toward an age of atomic-scale photonics. *MRS Bull.* **40**, 592–599 (2015).
44. Stier, A. V., Wilson, N. P., Clark, G., Xu, X. & Crooker, S. A. Probing the Iifluence of dielectric environment on excitons in monolayer WSe_2: Insight from high magnetic fields. *Nano Lett.* **16**, 7054–7060 (2016).
45. Raja, A. *et al.* Coulomb engineering of the bandgap and excitons in two-dimensional materials. *Nat. Commun.* **8**, 15251 (2017).
46. Gupta, G., Kallatt, S. & Majumdar, K. Direct observation of giant binding energy modulation of exciton complexes in monolayer $MoSe_2$. *Phys. Rev. B* **96**, 081403 (2017).
47. Stier, A. V. *et al.* Magnetooptics of exciton Rydberg states in a monolayer semiconductor. *Phys. Rev. Lett.* **120**, 057405 (2018).
48. Lloyd, D. *et al.* Band gap engineering with ultralarge biaxial strains in suspended monolayer MoS_2. *Nano Lett.* **16**, 5836–5841 (2016).
49. Aslan, O. B., Deng, M. & Heinz, T. F. Strain tuning of excitons in monolayer WSe_2. *Phys. Rev. B* **98**, 115308 (2018).
50. Ross, J. S. *et al.* Electrical control of neutral and charged excitons in a monolayer semiconductor. *Nat. Commun.* **4**, 1474 (2013).
51. Chernikov, A. *et al.* Electrical tuning of exciton binding energies in monolayer WS_2. *Phys. Rev. Lett.* **115**, 126802 (2015).
52. Yu, Y. *et al.* Giant gating tunability of optical refractive index in transition metal dichalcogenide monolayers. *Nano Lett.* **17**, 3613–3618 (2017).
53. Mak, K. F. & Shan, J. Mirrors made of a single atomic layer. *Nature* **556**, 177–178 (2018).
54. Back, P., Zeytinoglu, S., Ijaz, A., Kroner, M. & Imamoğlu, A. Realization of an electrically tunable narrow-bandwidth atomically thin mirror using monolayer $MoSe_2$. *Phys. Rev. Lett.* **120**, 037401 (2018).
55. Scuri, G. *et al.* Large excitonic reflectivity of monolayer $MoSe_2$ encapsulated in hexagonal boron nitride. *Phys. Rev. Lett.* **120**, 37402 (2018).
56. Krasnok, A., Lepeshov, S. & Alú, A. Nanophotonics with 2D Transition Metal Dichalcogenides. *Opt. Express* **26**, 2443–2447 (2018).
57. Tserkezis, C. *et al.* Mie excitons: Understanding strong coupling in dielectric nanoparticles. *Phys. Rev. B* **98**, 155439 (2018).
58. Yang, J. *et al.* Atomically thin optical lenses and gratings. *Light Sci. Appl.* **5**, e16046 (2016).

59. Liu, C.-H. *et al.* Ultrathin van der Waals metalenses. *Nano Lett.* **18**, 6961–6966 (2018).
60. Kong, X. T. *et al.* Graphene-based ultrathin flat lenses. *ACS Photonics* **2**, 200–207 (2015).
61. Zheng, X. *et al.* Highly efficient and ultra-broadband graphene oxide ultrathin lenses with three-dimensional subwavelength focusing. *Nat. Commun.* **6**, 8433 (2015).
62. Lin, H., Xu, Z.-Q., Qiu, C., Jia, B. & Bao, Q. High performance atomically thin flat lenses. *arXiv:1611.06457* (2016).
63. Georgiou, T. *et al.* Vertical field-effect transistor based on graphene–WS_2 heterostructures for flexible and transparent electronics. *Nat. Nanotechnol.* **8**, 100–103 (2012).
64. Shealy, D. L. & Hoffnagle, J. A. Laser beam shaping profiles and propagation. *Appl. Opt.* **45**, 5118–5131 (2006).
65. Li, Y. *et al.* Measurement of the optical dielectric function of monolayer transition-metal dichalcogenides: MoS_2, $MoSe_2$, WS_2, and WSe_2. *Phys. Rev. B* **90**, 205422 (2014).
66. Li, Q. T. *et al.* Free-Space Optical Beam Tapping with an All-Silica Metasurface. *ACS Photonics* **4**, 2544–2549 (2017).
67. Lien, D. H. *et al.* Electrical suppression of all nonradiative recombination pathways in monolayer semiconductors. *Science* **364**, 468–471 (2019).
68. Leighton, C. Electrolyte-based ionic control of functional oxides. *Nat. Mater.* **18**, 13–18 (2019).

III. Personnel and Training Opportunities

III. 1. Personnel Supported

At Stanford University, this program supported research in the group of Prof. Mark L. Brongersma (PI). At different times, the grant funded work by students Qitong Li and Aaron Holsteen as well as postdocs Dr. Jung-Hwan Song and Jorik van de Groep. Aaron Holsteen graduated and is now working at Apple. Qitong Li will graduate in one year from now. Dr. Song is now a senior scientist in my group and Dr. van de Groep started a faculty position at the University of Amsterdam in the Netherlands.

III.2. Research Training of Students

The training of graduate students was a critical aspect of this project. The sudden burst of activity in the field of metasurfaces and Augmented reality has led to hundreds of publications in the international literature and popular press. Major companies, such as Northrop Grumman, Apple, Advanced Materials, 3M, Samsung, Sony, Magic Leap, and Hewlett Packard now have active research efforts in these fields of study.

IV. Dissemination of Research findings

IV.1.Publications, Books, and Presentations

The research from this program led to a total of 10 publications in refereed journals, including 5 papers in Nature journals and 1 in Science Magazine. The PI also gives more than 15 invited talks (including several keynotes) each year on the topics related to this

program. He also incorporated the material from this program into a short courses taught at the CLEO conference every year on plasmonics and Mie-tronics. The students funded by this effort presented a number of contributed talks at International conferences.

Publications

1) "Subwavelength Angle-Sensing Photodetectors Inspired by Directional Hearing in Small Animals" Soongyu, Yi, Ming Zhou, Zongfu Yu, Pengyu Fan, Nader Behdad, Dianmin Lin, Shanhui Fan, and Mark L Brongersma, Nature Nanotechnology, 13, 1143–1147 (2018).
2) "Polarization-independent metasurface lens employing the Pancharatnam-Berry phase," Dianmin Lin, Aaron L. Holsteen, Elhanan Maguid, Pengyu Fan, Pieter G. Kik, Erez Hasman, Mark L. Brongersma, Optics Express 26, 24835-24842 (2018).
3) "Metasurface Mirrors for External Control of Mie Resonances," Jorik van de Groep, and Mark L .Brongersma, Nano Letters, 18, 3857-3864 (2018).
4) "Transparent multispectral photodetectors mimicking the human visual system," Qitong Li, Jorik van de Groep, Yifei Wang, Pieter G. Kik, Mark L. Brongersma, Nature Communication 10, 4982 (2019).
5) "Spatiotemporal light control with active metasurfaces," Amr M. Shaltout, Vladimir M. Shalaev, Mark L. Brongersma, Science 364, eaat3100 (2019).
6) "A Light-Field Metasurface for High-Resolution Single-Particle Tracking," Aaron L. Holsteen, Dianmin Lin, Isaac Kauvar, Gordon Wetzstein, Mark L. Brongersma, Nano Letters, 19, 2267-2271 (2019).
7) Mark Lawrence, David R. Barton III, Jefferson Dixon, Jung-Hwan Song, Jorik van de Groep, Mark L. Brongersma, and Jennifer A. Dionne, "High quality factor phase gradient metasurfaces. Nature Nanotechnology," 15, 956–961 (2020).
8) "An over-coupled phase-change metasurface for efficient reflection phase modulation," Junghyun Park, Soo Jin Kim, Patrick Landreman, Mark L. Brongersma,. Advanced Optical Materials 2000745, 1–8 (2020).
9) "Exciton resonance tuning of an atomically thin lens," Nature Photonics 14, 426–430 (2020).
10) "A high-quality-factor metasurface for rainbow-free optical eye tracking," Jung-Hwan Song, Jorik van de Groep, Soo Jin Kim, and Mark L. Brongersma, Accepted in Nature Nanotechnology

IV.2. Interactions and Transitions

This project has created a number of exciting opportunities for knowledge transfer. The work on integrated invisible detectors and spectro-polarimetry has attracted the interest of Metamaterials Technology Incorporated, Northrop Grumman, and Sony. This has led to several collaborations in this general area. The work on guided mode resonance metasurfaces also attracted interest from Magic Leap (an augment reality company) and Facebook. The work under this grant also impacted projects in the larger MURI programs on metasurfaces that were led by Professor Federico Capasso and Andrea Alu. Knowledge transfer also occurred via individual interactions, presentations, and short courses.

IV.3. Honors and Awards

Brongersma was elected as a Director-at-large of the Optical Society Board of Directors in 2016 and continued this role in 2017, 2018, and 2019. He was identified as a Highly Cited Researcher in 2018 and continues to be listed as one by Clarivate Analytics. He served as one of the Symposium Chairs for the Nanoscience + Engineering event at SPIE Annual Meeting (2018, 2019).